Variability in iron (II) oxidation kinetics across diverse hydrothermal sites on the northern Mid Atlantic Ridge

David González-Santana, Melchor González-Dávila, Maeve Lohan, Lise Artigue, Hélène Planquette, Géraldine Sarthou, Alessandro Tagliabue, J. Magdalena Santana-Casiano

HAL Id: hal-03212239

https://hal.univ-brest.fr/hal-03212239

Submitted on 22 Oct 2021

1 Variability in iron (II) oxidation kinetics across diverse hydrothermal sites on

2 the northern Mid Atlantic Ridge

3 David González-Santana[1]*, Melchor González-Dávila[2], Maeve C. Lohan[3], Lise Artigue[4],

4 Hélène Planquette[1], Géraldine Sarthou[1], Alessandro Tagliabue[5], J. Magdalena Santana-

5 Casiano[2]

6 [1]Univ Brest, CNRS, IRD, Ifremer, LEMAR, F-29280 Plouzane, France.

7 [2]Instituto de Oceanografía y Cambio Global, IOCAG, Universidad de Las Palmas de Gran

8 Canaria, Las Palmas de Gran Canaria, Spain.

9 [3]Ocean and Earth Science, University of Southampton, National Oceanography Centre,

10 Southampton, SO14 3ZH, United Kingdom.

11 [4]LEGOS, University of Toulouse, CNRS, CNES, IRD, UPS, 31400 Toulouse, France.

12 [5]School of Environmental Sciences, University of Liverpool, Liverpool, United Kingdom.

13 *** Correspondence:**

14 David González-Santana

15 david.gonzalezsantana@univ-brest.fr

18 **Abstract**

19 One of the recently recognized main sources of iron to the deep ocean inventory is the

20 hydrothermal activity associated with mid-ocean ridges. Little is known about the oxidation

21   kinetics of iron(II) within these environments, especially the dependence on physico-

22   chemical parameters such as temperature (T), pH, particle size-fractionation and the effect of

23   organic matter.

24   Following sample collection during the GA13 section cruise, the iron(II) oxidation at six

25   hydrothermal vent sites (Menez Gwen, Lucky Strike, Rainbow, Lost City, Broken Spur and

26   TAG) along the Mid-Atlantic Ridge were investigated, revealing high variability. The Fe(II)

27   oxidation rate constant analysis from multiple stations at two sites (Rainbow and TAG),

28   revealed that factors, other than T and pH, controlled the oxidation process. Experiments on

29   the effect of particle size-fractionation and organic matter at different pH showed that the

30   presence of organic ligands and colloidal size particles delayed the oxidation process, while

31   not affecting the overall pH dependency.

32   Extending our analysis to the broader relationship between the Fe(II) oxidation rate constants

33   across a range of temperatures (between 2 and 25 ºC) and pH (between 7 and 8) on a set of

34   selected hydrothermal samples allowed us to derive a multiparametric equation to model the

35   iron(II) oxidation rate constants in the ocean. This equation covers a larger range of

36   temperatures than previous published equations, improving its applicability for global

37   biogeochemical models.

38   1 Introduction

39   It is now well-established that phytoplankton growth is limited by the concentration of

40   dissolved iron (Fe) in up to 30% of the world oceans (Moore et al., 2013). Iron in the ocean,

41   can be found as both ferric (Fe(III)) and ferrous (Fe(II)) iron, where 99% of the dissolved

42   Fe(III) is complexed by organic ligands (Rue and Bruland, 1995). In oxic waters, Fe(II) tends

43   to oxidize to the most thermodynamically stable form, Fe(III), in a period of minutes to hours

44   (Santana-Casiano et al., 2005). Oxidation of Fe causes the solubility to decrease (Millero et

45   al., 1995), therefore, reducing its bioavailability (Shaked et al., 2005; Morel et al., 2008).

46   Recently, in the context of the international GEOTRACES program (www.geotraces.org),

47   several studies showed that Fe supplied by hydrothermal activity from mid-ocean ridges can

48   have a substantial impact on Fe distributions at basin scales (Tagliabue et al., 2010; Conway

49   and John, 2014; Resing et al., 2015; Fitzsimmons et al., 2017; Tagliabue et al., 2017).

50   Hydrothermal vent supply of dFe is required to reproduce deep ocean observations

51   (Tagliabue et al., 2010) could represent up to 11-22 % of the dissolved iron (dFe, filtered by

52   0.2 μm) present in the deep ocean globally (Bennett et al., 2008), accounting for a similar dFe

53   flux as continental riverine runoff (Elderfield and Schultz, 1996). Therefore,

54   hydrothermalism acts as an important Fe source in the deep ocean which may affect the

55   global biological carbon pump (Tagliabue et al., 2010; Resing et al., 2015).

56   The concentration of dissolved Fe(II) (dFe(II)) in the open ocean is very low, between 0.02

57   and 2 nmol L^{-1}, due to its fast oxidation under oxic conditions following the Fenton reaction

58   mechanism (González-Davila et al., 2005; Santana-Casiano et al., 2005). However, specific

59   oceanic regions present dFe(II) concentrations which are orders of magnitude higher. In

60   marine sediment interstitial waters, concentrations can reach around 300 μmol L^{-1} (de Baar

61   and De Jong, 2001), upwelling systems can increase Fe(II) concentrations up to 50 nmol L^{-1}

62   (Hong and Kester, 1986), while hydrothermal fluids can contain as much as 25 mmol L^{-1} of

63   dFe(II) (German and Von Damm, 2004). Water emanating from hydrothermal systems

64   contains high concentrations of Fe(II) amongst other elements (Mottl et al., 1979;

65   Mandernack and Tebo, 1993). Studies conducted at hydrothermal vent sites in different ocean

66   basins have revealed different Fe(II) oxidation rate constants, with Fe(II) half-life times

67   varying from 0.5 to 220 min, which has important implications for the dispersion of produced

68 Fe-oxide phases (Massoth et al., 1998; Field and Sherrell, 2000; Statham et al., 2005; Wang

69 et al., 2012; Santana-González et al., 2017; Rouxel et al., 2018). Recently, Gartman and

70 Findlay (2020) compiled all the available data for Fe(II) half-life from four hydrothermal

71 systems. One site was the TAG vent site in the Atlantic Ocean, while the others were located

72 in the Indian and Pacific Oceans, with Fe(II) half-life estimated using large Fe(II) spikes (500

73 nmol L^{-1}) that may affect the role played by different reactive oxygen species (González-

74 Dávila et al., 2006).

75 Temperature (T), pH, and oxygen concentration (O_2) are the primary variables known to

76 directly affect the Fe(II) oxidation (Stumm and Lee, 1961; Millero et al., 1987; Millero and

77 Sotolongo, 1989; Santana-Casiano et al., 2005). Salinity also affects the Fe(II) oxidation, as

78 reported in previous laboratory experiments (Millero et al., 1987; Santana-Casiano et al.,

79 2005). However, other factors such as changes in the inorganic complexation of Fe(II) due to

80 the specific ionic composition of the vent fluid, or organic complexation can influence these

81 oxidation rate constants (Rose and Waite, 2003; Statham et al., 2005). Therefore, the

82 oxidation rate constants must be termed "apparent" due to the effect of organic complexation

83 (Voelker and Sulzberger, 1996), as the nature and concentrations of organic ligands vary

84 between samples. Moreover, pyrite nanoparticles formed in hydrothermal vent sites, have

85 been estimated to oxidize more slowly than dissolved Fe(II) (Yücel et al., 2011), showing

86 that particle composition also influences the oxidation rate constants. The first empirical

87 equation describing the Fe(II) oxidation rate constants in seawater was reported by Millero et

88 al. (1987), and later updated by Santana-Casiano et al. (2005) for nanomolar concentrations.

89 This equation has been included in coupled physical-biogeochemical models in the ocean

90 (OGCBMs) to explore the impact of future climate change on the oxidation of Fe(II)

91 (Tagliabue and Völker, 2011). However, this equation was established for water temperatures

92 ranging from 10 to 25 ºC, which leads to discrepancies for the Fe(II) oxidation rate constants

93 for cold, deep ocean water masses.

94 The aims of this study were to measure the oxidation kinetic constants (k') of Fe(II) from

95 different hydrothermal vents and to investigate whether the variations of pH, T and S can

96 explain the observed variability, or if other factors such as the presence of particles, colloids

97 or dissolved organic matter (DOM) are significant contributors. This updated version of the

98 equation incorporates a wider range of temperatures, which lowers the error associated with

99 the theoretical Fe(II) oxidation rate constants. Thus, it becomes applicable to the calculation

100 of theoretical Fe(II) oxidation for the deep waters in which hydrothermal systems are

101 typically found.

2 Methods

2.1 Sampling sites and characteristics

104 Seawater samples were collected during the GA13 section cruise (JC156) along the Mid

105 Atlantic Ridge (MAR) onboard the *RRS James Cook*. This cruise departed Southampton, UK

106 on December 20th, 2017 and arrived into Guadeloupe, France on February 1st, 2018.

107 Alongside the large scale ocean section survey, sampling focused on six hydrothermal vent

108 sites along the MAR: Menez Gwen (37° 50'N 31° 31'W; Charlou et al., 2000), Lucky Strike

109 (37° 17'N 32° 16'W; Charlou et al., 2000), Rainbow (36° 14'N 33° 54'W; Douville et al.,

110 2002) , Lost City (30° 7'N 42° 7'W; Kelley et al., 2001), Broken Spur (29 °N; James et al.,

111 1995), and TAG (26°N; Gamo et al., 1996) (Fig. 1). These six hydrothermal vent sites

112 represent a wide range of possible hydrothermal conditions due to different underlying

113 geological conditions. Lost City and Menez Gwen are the shallowest sites, with the vent site

114 depths located at 700-720 m and 840-850 m, respectively. The Lucky Strike hydrothermal

115 field is situated between 1560 and 1730 m depth. The Rainbow vent site is found at 2270-

116 2280 m, within the average range (2000-3000 m) of oceanic ridge depth (Searle, 2013), while

117 Broken Spur and TAG are deeper hydrothermal systems located at 3100-3300 m and 3670-

118 3700 m, respectively. Chemically, Lost City is an alkaline hydrothermal vent, with pH

119 ranging from 9.0 to 9.8. The vent fluid is at a lower temperature of 40-75 °C, compared to

120 185-365 °C at the other vent sites and has extremely low concentrations of most trace

121 elements (e.g. Fe below the detection limit compared to 2-24000 $\mu mol\ L^{-1}$ at the other vent

122 sites) (Ludwig et al., 2006; Fouquet et al., 2013). All other hydrothermal vent sites are acidic

123 with pH lower than 4, and act as important sources of trace metals (Charlou et al., 2000;

124 Douville et al., 2002; Andreani et al., 2014). Geologically, Menez Gwen and Lucky Strike are

125 similar, their basement rocks are mafic, enriched-Mid-Ocean Ridge Basalt (E-MORB,

126 enriched with light rare earth elements, LREE), and present sulfide mounds. Rainbow also

127 presents sulfide mounds, but its basement rock is ultramafic. Further south, the alkaline Lost

128 City is also situated above an ultramafic base with carbonate chimneys. Finally, Broken Spur

129 and TAG have sulfide mounds and basement rocks formed by normal-MORB (N-MORB,

130 LREE depletion) (references within Fouquet et al., 2010).

131 Seawater samples were collected according to the GEOTRACES guidelines

132 (http://www.geotraces.org/images/Cookbook.pdf). Briefly, a titanium rosette fitted with 24 x

133 10 L trace metal-clean Teflon-coated OTE (Ocean Test Equipment) bottles, a CTD profiler

134 (Sea-bird Scientific), light scattering sensor (PMEL MAPR), and a redox potential sensor

135 (PMEL MAPR), were deployed on a conducting Kevlar wire to collect samples from the

136 water column. Sampling depths were actively chosen from the continuous T, salinity (S),

137 light scattering sensor (https://data-

138 search.nerc.ac.uk:443/geonetwork/srv/api/records/8ba648f2759d57fbb2246671f8065939)

139 and redox potential readings.

140　　Upon recovery, the OTE bottles were transported into an ISO class 6 clean air van. Unfiltered

141　　samples (UF) for Fe(II) oxidation kinetics were immediately transferred into thoroughly

142　　rinsed acid-cleaned 250 mL or 1 L low-density polyethylene bottles (LDPE; Nalgene)

143　　following the GEOTRACES Cookbook (http://www.geotraces.org/images/Cookbook.pdf)

144　　and frozen at -20 °C. Samples remained frozen in a -20 °C freezer for one year before their

145　　analysis. pH samples were collected in 125 mL borosilicate bottles and kept in the dark until

146　　the time of analysis.

147　　***2.2 pH determination***

148　　pH was measured onboard and during laboratory-based kinetic experiments in the free scale

149　　using a Tris buffer solution (Millero, 1986). Onboard pH samples were kept in the dark,

150　　inserted into a 25 °C water bath, and measured at 25 °C, within less than 1 hour after

151　　collection. Laboratory-based kinetic experiments used a Titrino 719 (Metrohm^{TM}) which

152　　automatically added 0.01M hydrochloric acid (HCl, PANREAC Hiperpur-plus) in order to

153　　keep the pH constant. The pH at *in situ* conditions were computed considering the total

154　　alkalinity for an average profile of the area (Key et al., 2015; Olsen et al., 2016). The average

155　　profile was obtained from plotting all the available alkalinity data from the studied region

156　　(20-30 °N and 40-50 °W). The associated error of the estimate was ±6 μmol kg^{-1}. Gray et al.

157　　(2011) showed that computed pH values are relatively insensitive to errors in alkalinity, and

158　　that pH measurements can be used to compute the magnitude and variability of inorganic

159　　carbon variables. A fluctuation of 400 μmol kg^{-1} in total alkalinity values (e.g. from 2325 to

160　　2725 μmol kg^{-1}) will change the pH in +0.005, which lies within the error of determination

161　　for potentiometric pH. The set of constants from Lueker et al. (2000) were used.

162　　All the pH data in the text and in the figures, including kinetics and profile data are expressed

163　　in the free scale.

2.3 Fe(II) measurements

165 In order to measure the Fe(II) oxidation rate constants, continuous Fe(II) concentrations were

166 determined using the FeLume System (Waterville Analytical), with a data point acquisition

167 every 1 s. This direct Flow Injection Analysis system uses luminol (5-amino-2,3-dihydro-1,4-

168 phthalazinedione, Sigma-Aldrich) as the reagent (King et al., 1995) which reacts with Fe(II).

169 The sample was continuously aerated with pure air (Carburos Metalicos S.A.). A 0.8 nmol L^{-1}

170 addition of Fe(II) (ammonium iron(II) sulfate hexahydrate, Sigma-Aldrich) was introduced

171 into each sample and the Fe(II) concentration was continuously monitored until the signal

172 had reduced by 70 %. This method produces apparent rate constants (k_{app}) because the

173 oxidation rate constant is measured on a Fe(II) spike rather than on the ambient Fe(II).

174 Although, the oxidation rate constant is not affected by the initial Fe(II) in solution (Millero

175 et al., 1987; Roy et al., 2008; Roy and Wells, 2011; Santana-González et al., 2018), the

176 equilibrium with the organic ligands and particle surfaces could be affected. Moreover, due to

177 the effects of organic complexation and that the concentrations of the organic ligands in each

178 sample are not constant, the apparent oxidation rate constants are consequently not true

179 constants.

180 Some previous oxidation kinetic studies have found a second-order dependency of the Fe(II)

181 concentration against time (e.g. Statham et al., 2005). However, in oxygen saturated samples

182 a pseudo-first order rate dependency was obtained, where the slope (ln([Fe(II)] against time)

183 represents the pseudo-first order rate constant *k'* (Eq. 1). The linearity remained longer than

184 the half-life time and was thus considered acceptable in all the analyses ($R^2 = 0.983 \pm 0.017$,

185 n samples = 298). The observed linearity confirms that the equilibrium between the added

186 Fe(II) with organic ligands and particles is achieved before 30 s (our first Fe(II)

187 determination time limit). The *k'* error associated with these high R^2 values was 2% for *in*

188   *situ* condition experiments, and 1% for experiments carried out at 25 °C. The half-life ($t_{1/2}$) of

189   Fe(II) in seawater can be calculated from k' (Eq. 1 and 2).

190     $$d[Fe(II)]/dt = -k_{app}[O2][Fe(II)]$$ (1)

191   In oxygen saturated concentrations, the corresponding pseudo-first order rate constant $k' =$

192     $k_{app}[O_2]$.

193     $$t_{1/2} = \ln(2)/k'$$ (2)

194   The minimum energy required to start the oxidation reaction (activation energy, E_a, J mol^{-1})

195   and the corresponding preexponential or frequency factor (A) were computed from the

196   calculated k' using the empirical Arrhenius equation, where R is the universal gas constant

197   (8.314 J mol^{-1} K^{-1}):

198     $$\log(k') = \log(A) - \frac{E_a}{R \cdot \ln(10) \cdot T}$$ (3)

199   Iron (II) blanks were obtained from a 2 h aerated, magnetically stirred sample which was kept

200   in the dark to achieve the oxidation of Fe(II) (Santana-Casiano et al., 2005). Iron (II) in theses

201   blanks always below the detection limit. Calibration curves (0 to 1 nmol L^{-1}) were produced

202   daily and confirmed linearity in the Fe(II) signal. The detection limit, defined as three times

203   the standard deviation of the blank after being aerated for 10 minutes, was lower than 50

204   pmol L^{-1}. Reproducibility was checked by running the same sample three times throughout

205   the day after an addition of 1nmol L^{-1} of Fe(II) with an agreement in concentrations that was

206   better than ± 0.1 nmol L^{-1}. Accuracy could not be determined since reference materials

207   currently do not exist. Results are systematically given as $t_{1/2}$ (in min), followed by the

208   measured k' (in min^{-1}).

209   **2.4 Experimental setup**

210   Using natural seawater samples, kinetic experiments were carried out under different

211   conditions, with pH and T set to *in situ* conditions (data shown in the supplementary Table

212   S1), and with pH and T normalized to constant values, in unfiltered, filtered and filtered and

213   UV-irradiated samples. These later experiments required a high sample volume, limiting the

214   number of experiments.

215   The steps required for the Fe(II) oxidation kinetics determination are as follows. The day

216   before the experiments, three to four frozen samples were taken out of the freezer and placed

217   in a fridge set to 4 ˚C. The next morning, a temperature-controlled water bath was set to the

218   coldest *in situ* potential temperature (supplementary Table S1). While the water bath was

219   cooling down, each sample was subsampled into three 60 mL acid cleaned LDPE bottles and

220   placed back into the fridge. One of the subsamples was inserted into the temperature-

221   controlled water bath, which was set to the original *in situ* potential temperature of the

222   sample. The sample was left in the water bath for acclimatization during 15 min and then

223   transferred into the reaction vessel. In the reaction vessel, the sample was aerated prior to and

224   during the study. After 10 minutes of aeration, the Fe(II) addition was made and the Fe(II)

225   concentration and time were continuously monitored. After finishing with the coldest

226   subsample, the temperature of the water bath was increased to the following coldest

227   temperature, and the next sample was left to acclimate.

228   ***2.4.1 Quantification of the temperature and pH effect on the iron (II) oxidation rate***

229   ***constant***

230   In order to improve the temperature range of the existing Fe(II) oxidation kinetic equation, 1

231   L samples of deep ocean water were collected during the JC156 cruise, at stations 13 (2339

232   m), 16 (2051 m), 24 (2829 m), 30 (2700 m), 31 (2796 m), and 35 (1999, 3350 and 3601 m).

233   The samples remained frozen at -20 °C during one year until analysis. Two days prior to the

234   analysis, samples were thawed in a 4 °C fridge. This allowed a slow melting of the samples in

235   the dark, thus limiting any photoproduction of Fe(II) and also removal of any superoxide and

236   hydroxyl radicals in the sample (Voelker and Sedlak, 1995).

237   The samples were then transfered into 60 mL LDPE bottles (one for each condition).

238   Temperature effect experiments were performed at constant pH, and those for pH effect at

239   constant temperature. The temperature effect experiments were carried out at *in situ*

240   temperature, 10, 20 and 25 °C at a fixed pH of 8. The pH effect experiments were carried out

241   at *in situ* pH, and pH 7, 7.5 and 8 at a fixed temperature of 25 °C.

242   ***2.4.2 Oxidation rate constants through the water column at the six hydrothermal vent sites***

243   To assess the expected Fe(II) oxidation rate constants at *in situ* conditions, the experiments

244   were carried out at *in situ* potential temperature and pH ($T_{is}pH_{is}$). The temperature was then

245   increased to 25 °C ($T_{25}pH_{is}$) to obtain the temperature effect on the oxidation rate constants.

246   A third set of experiments were performed at 25 °C and pH 8 ($T_{25}pH_8$). The T and pH

247   normalization of all the samples allowed for the interpretation of the effect of other variables,

248   such as organic matter and particles, in the oxidation rate constants. This allows to investigate

249   where seawater composition is influencing the oxidation rate, a process that cannot be

250   isolated when comparing two samples with different temperatures and/or pH.

251   ***2.4.3 Experimental setup to assess the effect of colloidal and organic matter***

252   The unused unfiltered (UF) sample volumes remaining from the quantification of the

253   temperature and pH effect experiments were used to assess the impact of particles, colloids

254   and organic matter. Unfiltered samples underwent sequential filtration. Three aliquots were

255   filtered through 0.2 μm (F0.2; Whatman® Anodisc), and one of them was then filtered

256   through 0.02 μm (F0.02; Whatman® Anotop®), while the last aliquot was filtered through

257   0.02 μm followed by UV-irradiation (F0.02+UV). All samples were left in the dark for 6

258   days to limit the effect of any photochemically generated reactive oxygen species (ROS)

259   produced during the UV-irradiation (Yuan and Shiller, 2001; Roy et al., 2008). All samples

260   were analyzed following the same procedure as for the assessment of the pH effect (see

261   section 2.4.2 above). In order to assess whether the generated ROS species could affect the

262   Fe(II) oxidation rate constants determined after 0.02 μm filtration and UV-irradiation, the

263   effect of the amount of hydrogen peroxide (H_2O_2) generated during this process was

264   considered (Yuan and Shiller, 2001; O'Sullivan et al., 2005). Other short-lived ROS species

265   such as hydroxyl radicals were not accounted for, since their nanosecond half-life times do

266   not allow for their determination using our analytical method.

267   3 Results

268   *3.1 Temperature and pH effects on the oxidation rate* constant*s*

269   Experiments for the temperature effect study were carried out at a pH of 8. When plotting log

270   k' vs. $1/T$ (K^{-1}) (Fig. 2, Eq. 3), results showed an average slope ($-\Delta E_a/R/\ln(10)$) of $-4992 \pm$

271   232. Notably, the data obtained from samples collected west of TAG at 2700 m depth

272   (Station 30) showed a slope of -3732 ± 216, which is more than three standard deviations

273   away from the average value. This lower slope corresponds to a much lower activation

274   energy for this sample, with a value of 71 ± 4 KJ mol^{-1}. This effect was probably caused by

275   the interaction of organic compounds or particles with the Fe(II) species which affected the

276   limiting Fe(II) oxidation step, and therefore a result of a different oxidation reaction

277   mechanism. If this sample is removed, the average slope increases to -5434 ± 183, and the

278   activation energy of all the samples considered was 104 ± 3 KJ mol^{-1}. These values are within

279   the experimental error of previous determinations from Gulf Stream water (-5362 ± 162, and

280   an activation energy of 103 ± 3 KJ mol^{-1} ; Santana-Casiano et al., 2005).

281   When experiments were carried out at a constant T of 25 ºC and at 5 different pH values in

282   the range from 7 to 8, log *k'* and pH were linearly related, with slopes of 1.00 ± 0.06 (Fig. 3)

283   and with no data points outside of 3standard deviations. As with the temperature relationship,

284   the sample from the station West of TAG at 2700 m presented a slope (1.19 ± 0.08) out of the

285   1:1 dependence. A second sample, (TAG at 1999 m depth, over 1600 m above the vent site)

286   showed a lower slope (0.81 ± 0.12).

287   The unique use of lower temperature samples in this study, allowed a better estimation of

288   Fe(II) oxidation kinetic rate constants at temperatures lower than 10 ºC, increasing the range

289   of applicability of the Fe(II) oxidation kinetic equation of Santana-Casiano et al. (2005).

290   Using the equation and dataset from Santana-Casiano et al. (2005), which had a wider range

291   in pH and salinity, together with the additional pH data and a wider range of temperature

292   from the present study, a revised equation was obtained. The pH and salinity dependence did

293   not change, while the T relationship was modified (Eq. 4). Thus, an updated equation for the

294   theoretical Fe(II) oxidation appropriate for deep waters is presented:

295     $\log k'(s^{-1}) = 35.627 - 6.7109 * pH + 0.5342 * pH^2 - 5434.02/T - 0.04406 * S^{1/2} -$

296     $0.002847 * S$ (4)

297   The T factor has been modified from -5362.6/T to -5434.02/T obtained from the average

298   slope of Figure 2. To assess the performance of the updated Fe(II) oxidation kinetic equation

299   (Eq. 4), it was compared to three existing equations. The chosen equations were the first

300   derived equation (Millero et al., 1987), the equation by Santana-Casiano et al. (2005), and a

301   recent equation using Labrador Seawater (Santana-González et al., 2019). The four equations

302   were compared to the measured oxidation rate constants at *in situ* pH and T conditions. The

303   residual sum of squares (RSS) and root mean square error (RMSE) between predicted and

304   observed values were calculated. Smallest values of RSS and RMSE indicate the best

13

equation fit to observations. Additionally, the difference in logarithms of the likelihood

(Δlog(L)), based on a Gaussian error distribution with a constant variance of log-transformed

data, was used to compare the equation performance (Armstrong et al., 2001 and references

therein). The log(L) was calculated as in Moriceau et al. (2009), where a difference in log(L)

of at least two points is considered as a criterion of a better fit to the observations. The three

most recent equations present better RSS, RMSE and log(L), with the new equation presented

here providing consistently better statistical results (Table 1).

	Millero et al. (1987)	Santana-Casiano et al. (2005)	Santana-González et al. (2019)	González-Santana et al. (Eq. 4 of this manuscript)
RSS	0.019	0.003	0.006	0.002
RMSE	0.019	0.008	0.011	0.007
log(L)	24.2	33.6	32.5	36.7

Table 1. Statistical comparison of the available Fe(II) oxidation kinetic equations with the

measured oxidation rate constants for deep ocean waters without including the hydrothermal

neutrally buoyant plumes. Low residual sum of squares (RSS) and root mean square error

(RMSE) indicate the best equation fit to observations. Greater than two points of difference

in the difference in logarithms of the likelihood (Δlog(L)) presents a better fit.

3.2 Iron(II) oxidation rate constants throughout hydrothermal plumes along the MAR

Figures 4 and 5 present the half-life times of Fe(II) samples collected above each

hydrothermal site with Figure 5 summarizing the results using boxplots. The measured $t_{1/2}$

320 values presented a wider range than those determined using the physico-chemical parameters

321 in the improved theoretical equation. The Lost City vent site, was the only station where all

322 the measured $t_{1/2}$ at $T_{is}pH_{is}$ conditions presented measured oxidation rate constants higher

323 (shorter $t_{1/2}$) than the theoretically calculated rate constants. At $T_{25}pH_8$ conditions, all the

324 measured oxidation rate constants were higher than the theoretical ones for all stations except

325 at TAG.

326 The theoretical $t_{1/2}$ values presented in Figure 5a, show the expected high variability in the

327 Fe(II) half-life times associated with T, pH and S. These discrepancies were further

328 highlighted in the measured samples, where only Menez Gwen and Lucky Strike theoretical

329 values are within the measured results (a paired t-test did not show a statistical difference

330 between the theoretical and the measured $t_{1/2}$, with P > 0.35 for both).

331 At Menez Gwen (Fig. 4a), measured *in situ* $t_{1/2}$ varied between 8.3 and 32.0 min (*k'* between

332 0.084 and 0.022 min^{-1}), with short measured $t_{1/2}$ observed in the samples collected at 743,

333 821, and 827 m. When the temperature was increased and fixed to 25 ºC, while the pH was

334 kept at *in situ* conditions (Supplementary Table S1), a significant T effect was observed in *k'*,

335 with the measured $t_{1/2}$ decreasing to less than 4 min. When the pH was fixed to a constant

336 value of 8 along the water column, the measured $t_{1/2}$ was slightly affected indicating a small

337 effect, as the change in pH was always lower than 0.22. Overall, at T_{25}, samples presented

338 measured $t_{1/2}$ in the same order of magnitude as the theoretical $T_{25} pH_8$. Samples collected

339 within the lower part of the plume, at less than 30 m above the seafloor (hereafter *asf*)

340 presented higher oxidation rate constants than theoretical ones ($t_{1/2}$ decreased).

341 Lucky Strike (Fig. 5a) presented lower oxidation rate constants than Menez Gwen related to

342 lower temperatures in deeper waters (from about 8.5 ºC to 4.5 ºC). From 1600 m to 1680 m,

343 measured $t_{1/2}$ averaged 46.5 ± 2.5 min (*k'* of 0.015 ± 0.001 min^{-1}, n = 4) (Fig. 4b). This $t_{1/2}$

344   average is higher than the theoretical value of 39.7 min, while at 1703 m, the Fe(II) half-life

345   decreased to 26.3 min (k' to 0.026 min^{-1}). Overall, at T_{25}, samples presented measured $t_{1/2}$ in

346   the same order of magnitude as the theoretical T_{25} pH$_8$. *In situ* pH averaged 7.89, where the

347   increase in acidity produced a lower oxidation rate constant than the measured $t_{1/2}$ at T_{25} pH$_8$.

348   At Rainbow, station 16, the $t_{1/2}$ measured at *in situ* conditions presented a wide range of

349   variation, from 17.3 to 65.3 min (k' varied from 0.040 min^{-1} to 0.011 min^{-1}). The theoretically

350   expected values were within that range, with an average value of 39 ± 3 min (n=8, Fig. 4c).

351   The shortest $t_{1/2}$ were observed between 1986 m and 2108 m (175 to 295 m *asf*) averaging

352   22.2 ± 3.6 min ($k' = 0.032 \pm 0.006$ min^{-1}) while the shorter $t_{1/2}$ were found below the plume

353   and above 300 m *asf* (Fig. 4c). The light scattering data shows that the Rainbow plume

354   reached heights over 400 m *asf* (although samples were only collected within the first 330 m).

355   Temperature was an important factor controlling the oxidation rate constant. At T_{25}

356   conditions $t_{1/2}$ were similar to the theoretical value. When the pH was fixed to 8, small

357   changes were observed, and most of the values were close to the theoretical value except for

358   those around 1986 m and 2108 m which had shorter $t_{1/2}$.

359   Lost City (Fig. 4d), the only alkaline hydrothermal vent, was drastically different from the

360   other hydrothermal sites (Fig. 4d), with temperatures around 10 ºC and pH$_{is}$ of 8.07

361   (Supplementary Table S1). The theoretical $t_{1/2}$ associated with these temperatures and pH

362   ranged between 16 and 20 min. However, most of the measured $t_{1/2}$ were shorter than 3 min,

363   reaching 0.5 min (k' of 1.299 min^{-1}) at 725 m with the longest $t_{1/2}$ of 7.8 min (k' of 0.088 min^{-}

364   ^{1}) at 750 m. At 750 m depth with T_{25}pH$_{is}$ conditions, the $t_{1/2}$ decreased to 1.9 min (k' of 0.357

365   min^{-1}) and further decreased to 1.5 min (k' of 0.468 min^{-1}) at T_{25}pH$_8$ conditions. All the

366   measured $t_{1/2}$ were significantly shorter than the theoretical $t_{1/2}$ of 3.2 min (k' of 0.218 min^{-1})

367   at normalized conditions.

368   Broken Spur presented a wide range in measured $t_{1/2}$, with values under *in situ* conditions

369   ranging from 1.0 to 65.1 min (k' ranging from 0.714 min^{-1} at 2929 m to 0.011 min^{-1} at 2858

370   m; Fig. 4e). Two different behaviors can be observed. The two shallowest samples (2820 and

371   2830 m) were collected in local light scattering minima, with $t_{1/2}$ averaging 63.2 ± 2.7 min (k'

372   of 0.011 ± 0.001 min^{-1}) and values slightly higher than the theoretical ones. Deeper than 2830

373   m, the samples were collected in local light scattering maxima, where half-life times were

374   shorter with an average $t_{1/2}$ of 1.9 ± 1.2 min (averaged k' of 0.464 ± 0.220 min^{-1}).

375   Experiments at $T_{25}pH_8$ also showed that samples below 2830 m presented shorter $t_{1/2}$ (high k'

376   values) than what was theoretically expected.

377   Half-life times measured at *in situ* conditions from the TAG vent site samples presented the

378   widest range in $t_{1/2}$ (Figs. 4 and 5a), varying from 35.1 to 131.2 min (k' between 0.019 min^{-1}

379   and 0.005 min^{-1}). These samples were characterized by little variability of T_{is} (2.67 ± 0.01 ºC)

380   and pH_{is} (8.17 ± 0.01), producing a stable theoretical $t_{1/2}$ of 43 ± 2 min. Furthermore, the

381   measured $t_{1/2}$ were the longest obtained in these experiments. When the experiments were

382   repeated at both fixed T_{25} and pH_8 the measured values encompassed the theoretical value of

383   3.3 min, with values slightly higher at around 3325 m (4.3-4.4 min). Therefore, even when

384   temperature and pH affected the observed oxidation rate constants, the high range of values at

385   *in situ* conditions could not be explained by only these two physico-chemical variables.

386   ***3.3 Investigating the spatial variability of Fe(II) oxidation rate* constants *around Rainbow***

387   ***and TAG sites***

388   To investigate the spatial variability in $t_{1/2}$ for Fe(II), samples were collected from four

389   stations around the Rainbow site at 0.3º (30 km) S (St 15), E (St 12) and W (St 13) and 1º

390   (120 km) E (St 10) (Fig. 1) and from five stations around TAG at 0.3º N (St 26), S (St 27), W

391   (St 30), and E (St 31) and 1º W (St 29) (Fig. 1). At both vent sites, turbidity and light

392   scattering anomalies matched and described the shape of the plume (gray shading in Fig. 4).

393   The Rainbow plume anomaly was observed between 1930-1995 m, 2060-2090 m, and most

394   strongly between 2100 and 2210 m. At the TAG site, the signal was three times lower than

395   that observed at Rainbow, indicating the presence of a lower amount of particles, which could

396   also be due to a displacement of the sampling with respect to the vent site. The largest

397   anomalies were measured between 3160-3390 m, with several minor anomalies above (e.g.

398   2980-3030 m) and below (e.g. 3430-3520 m and 3600-3625 m; Fig. 4).

399   Turbidity and light scattering were useful for tracking the plume displacement even at 30 km

400   from the vent site. The Rainbow plume was observed to the south and west (Stn. 13 and 15)

401   at depths between 2000 and 2040 m, and 2270 and 2300 m. For TAG, only stations 27 (south

402   of TAG, but inside the MAR valley) and 31 (east) showed deeper and thinner turbidity

403   anomalies between 3400 and 3690 m and a smaller signal between 2920 and 3060 m.

404   For the Rainbow field, samples collected at the vent site in the 1980-2150 m range had

405   shorter $t_{1/2}$ at *in situ* conditions (high k' values) than the theoretical $t_{1/2}$ (Fig. 6a). All the other

406   samples (except for Stn 10 at 2430 m) had higher $t_{1/2}$ values than those calculated

407   theoretically, and greater $t_{1/2}$ than observed at Rainbow at depths shallower than 1980 m,

408   indicating very low oxidation rate constants. This allowed Fe(II) to stay in solution three

409   times longer than under inorganic seawater conditions. However, when T and pH were fixed

410   (Fig. 6b), the oxidation rate constants between stations were much closer to the theoretical

411   value, indicating the T and pH control over the Fe(II) oxidation rate constant. Nevertheless,

412   plume samples at the 2100-2210 m range and around 2400 m indicated $t_{1/2}$ values that were

413   still at least double the theoretical value.

414   At the TAG hydrothermal field, stations situated towards the N and W of TAG presented

415   shorter $t_{1/2}$ (high k' values) than those at the vent site and towards the S and E (Fig. 7a).

18

416   Station 30, situated 30 km W of TAG, exhibited both patterns, with long $t_{1/2}$ (low k' values) at

417   depths shallower than 2600 m and short $t_{1/2}$ (high k' values) at depths below 2700 m. When

418   all the TAG hydrothermal field station samples were normalized (i.e. $T_{25}pH_8$; Fig. 7b), most

419   of the variability was removed, and $t_{1/2}$ averaged 3 ± 1.5 min. The same pattern as for *in situ*

420   conditions was maintained, with stations situated towards the N and W having shorter $t_{1/2}$

421   than the theoretical values. These three stations were characterized by their lower turbidity in

422   the deep waters.

3.4 The effect of particles, colloids, and organic matter on oxidation rate constants

424   Experiments with samples from Rainbow (Stn 16, 2051 m), West of Rainbow (Stn 13, 2339

425   m), Broken Spur (Stn 24, 2829 m) and TAG (Stn 35, 3350 m) were performed to improve our

426   understanding of the impact of particulate and organic matter on the oxidation kinetics of

427   hydrothermal vent fluids. The Rainbow sample at 2051 m, located outside the plume, did not

428   show any difference in the $\log(k')$ due to the presence of particulates, with values at each pH

429   unit varying by ± 0.03 and an average slope of $\log(k')$ against pH of 0.96 ± 0.07 for UF, F0.2

430   and F0.02 treatments (Fig. 8). For the other three samples (Figs. 8b-d), oxidation rate

431   constants for UF and F0.2 did not present significant differences, with values that were

432   reproducible within ±0.02 for the studied pH range. However, F0.02 samples had higher

433   oxidation rate constants, while also maintaining the pH dependence (0.95 ± 0.07). Therefore,

434   the presence of colloidal size particles delayed the oxidation process while not affecting the

435   pH dependence, as shown in Fig. 8, where the intercept changes but the slope is unchanged.

436   All of the UV irradiated samples in Figs. 8a-d indicate that the absence of dissolved organic

437   matter increased the oxidation rate constants. For TAG (3350 m) and Rainbow (2051 m), the

438   k' values were so high that it was impossible to determine them at pH = 8 under our

439   experimental conditions.

4 Discussion

4.1. Derived oxidation rate constants as a function of pH and temperature

In the 1990s, Fe(II) oxidation kinetics variability was reported at the TAG hydrothermal field (2-3 min) (Rudnicki and Elderfield, 1993) and near the Juan de Fuca Ridge hydrothermal systems (32 h) (Chin et al., 1994; Massoth et al., 1994) using the Millero et al. (1987) equation. Nevertheless, the variability between those two sites was difficult to explain and reflected fluctuations caused by differences in O_2, T, and pH among the different sites.

When combining the six hydrothermal vent sites on the MAR (Fig. 9), the relationship between the measured oxidation rate constants under *in situ* conditions against the theoretically derived oxidation rate constants as a function of pH and temperature (in aerated water) can be obtained. Overall, equation 4 can explain 76 out of 104 data points. When color-coding the data points by stations, we observed that all the outliers corresponded to samples that were collected inside hydrothermal plumes (defined by turbidity, light scatter, and redox potential). Consequently, the results obtained from the theoretical equation (Eq. 4) and figure 9, agree well with previous results that O_2, S, T, and pH can be used to characterize the Fe(II) oxidation rate constant in open ocean waters but not from within hydrothermal plumes.

Our study clearly indicates (Figs. 8 and 9) that the presence of both colloidal particles and dissolved organic matter increases the half-life of Fe(II) (decreased *k'*). This agrees with previous work showing a decrease in the Fe(II) oxidation rate constants in seawater in the presence of some natural organic compounds (Santana-González et al., 2019). However, organic matter can have a positive or negative effect on the oxidation rate constants of Fe(II) depending on the type of organic matter and its degree of remineralization (Rose and Waite,

463   2003). The variability in the effect of total organic carbon on Fe(II) oxidation proves that

464   total organic carbon cannot be used as a variable in an equation describing k' (Santana-

465   Casiano et al., 2000; Santana-González et al., 2018; Santana-González et al., 2019). In this

466   sense, a more detailed characterization of organic matter would be necessary, especially in a

467   hydrothermal environment.

468   *4.2. Influence of organic species on Fe(II) oxidation rate constants*

469   The Fe(II) oxidation rate constant (Eq. 5) can be expressed as a function of each Fe(II)

470   species (Fe^{2+}, $FeOH^+$, $Fe(OH)_2$, $FeHCO_3^+$, $Fe(CO_3)$, $Fe(CO_3)_2^{2-}$, $Fe(CO_3)OH^-$, $FeCl^+$, $FeSO_4$,

471   FeH_3SiO_4 and any organically complexed Fe species). Species such as $Fe(CO_3)_2^{2-}$ and

472    $Fe(OH)_2$ could become important at pH higher than 8 (Ussher et al., 2004; González-Davila

473   et al., 2005; Santana-Casiano et al., 2005) in solution. Considering the side reaction

474   coefficient for each inorganic (α_i) and organic (α_j) Fe(II) species in seawater and the

475   associated second-order oxidation rate constant for the kinetically reactive Fe(II) species (k_i

476   and k_j) (Eq. 6) (Millero and Sotolongo, 1989; King, 1998; Santana-Casiano et al., 2005), the

477   apparent oxidation rate constant can be expressed as:

478    $k_{app} = k_{Fe^{2+}}\alpha_{Fe^{2+}} + k_{FeOH^+}\alpha_{FeOH^+} + k_{Fe(OH)_2}\alpha_{Fe(OH)_2} + k_{FeHCO_3^+}\alpha_{FeHCO_3^+} +$

479    $k_{Fe(CO_3)}\alpha_{Fe(CO_3)} + k_{Fe(CO_3)_2^{2-}}\alpha_{Fe(CO_3)_2^{2-}} + k_{Fe(CO_3)OH^-}\alpha_{Fe(CO_3)OH^-} + k_{FeCl^+}\alpha_{FeCl^+} +$

480    $k_{FeSO_4}\alpha_{FeSO_4} + k_{FeH_3Si\ _4}\alpha_{FeH_3SiO_4} + \sum_j k_{FeL_j}\alpha_{FeL_j}$ (5)

481    $k_{app} = \sum_i \alpha_i k_i + \sum_j \alpha_j k_j$ (6)

482    $\alpha_{Fe^{2+}} = 1/\left(1 + \sum K_{L_i}[L_i] + \sum K_{L_j}[L_j]\right)$ (7)

483   Where $\alpha_{Fe^{2+}}$ is the fraction of free Fe(II) including inorganic and organic speciation, $[L_i]$ is

484   the concentration of each inorganic ligand with a conditional stability constant K_i and $[L_j]$ is

21

485   the concentration of each organic ligand with a conditional stability constant K_{Lj}. The

486   inorganic site reaction coefficient at pH 8 and 25 ºC was previously determined as 0.38

487   (Santana-Casiano et al., 2006). For any inorganic or organic FeL complexes:

488    $\alpha_{FeL} = K_{FeL}[L]\alpha_{Fe^{2+}}$ (8)

489   According to our results, the presence of DOM in solution generated Fe(II)-organic

490   complexes that were overall less reactive to oxidation and therefore, when removed by UV

491   irradiation the resulting oxidation rate constants were higher (Fig. 8).

492   The amount of dissolved organic carbon (DOC) in the samples ranged between 50 and 79

493   μmol kg^{-1} (data not shown) and according to O'Sullivan et al. (2005) the maximum amount

494   of H_2O_2 produced during irradiation could be 125 to 147 nmol kg^{-1}, respectively. Following

495   González-Davila et al. (2005) and assuming the extreme case of no H_2O_2 decay after 6 days,

496   the UV generated H_2O_2 could theoretically increase the Fe(II) oxidation rate constants in

497   oxygen saturated conditions. The theoretical $t_{1/2}$ associated with the H_2O_2 oxidation was

498   between 48 % and 53 % of the $t_{1/2}$ measured for 0.02 μm filtered samples. Nevertheless, the

499   measured $t_{1/2}$ for UV-irradiated samples (Supplementary Table S1 and Fig. 8) were shorter

500   (higher k'), indicating that any H_2O_2 remaining in solution after 6 days was not the main

501   factor that increased the oxidation rate constants and that the presence of dissolved organic

502   matter was stabilizing Fe(II) in solution. Furthermore, laboratory experiments have shown

503   that the $t_{1/2}$ of H_2O_2 in oceanic waters is shorter than 5.5 days (Yuan and Shiller, 2001),

504   therefore the impact of H_2O_2 in the experiments would be further reduced.

505   The role of organically complexed Fe(II) could be calculated from the following

506   assumptions. Firstly, the Fe(II)-L complex was assumed to not oxidize in the pH range of 7.5

507   to 8. Secondly, the observed reduction in Fe(II) oxidation rate constants (Fig. 8 and

508   Supplementary Table S1) at 25 ºC between the 0.02 μm filtered and the filtered and UV

509   irradiated samples was due to organic complexation. The computed role of organic

510   complexation produced a $78 \pm 6\%$ decrease in the concentration of reactive inorganic Fe(II)

511   species. The effect of organic Fe(II) species was highest at Broken Spur and TAG sites ($81 \pm$

512   5%) and lowest at Rainbow ($74.1 \pm 4 \%$). Roy et al. (2008) found a value that was slightly

513   lower for the western subarctic Pacific water, with a $61 \pm 8\%$ decrease. As both the organic

514   ligand concentrations and the conditional constants are unknown, only the product $K_{Lj} \cdot \left[L_j\right]$

515   (Eq. 7) can be inferred. Knowing the inorganic distribution coefficient of Fe(II), which is pH

516   dependent but can be calculated from Santana-Casiano et al., (2005), and considering a

517   unique class of ligand (L), the product $K_{Lj} \cdot \left[L_j\right]$ should be 9 ± 2 (higher values at Broken Spur

518   and TAG, while lower values at Rainbow) while $1 + \sum K_{L_i}[L_i]$ in Eq. 7 is 2.6 ($2.6 = 1/0.38$,

519   Santana-Casiano et al., (2006)).

520   If the concentration of Fe(II) organic ligands in seawater is on the same order as Fe(III)

521   ligands (1 to 10 nmol L^{-1}), as assumed by Roy et al. (2008), the corresponding conditional

522   constant should range between 10^9 to 10^{10}, (respectively for 10 and 1 nmol L^{-1} of ligands).

523   The strength of these Fe(II) complexing ligands compared to those for Fe(III) is in the low

524   affinity range (Gledhill and Buck, 2012; Bundy et al., 2014). However, the formation of these

525   complexes would decrease the Fe(II) oxidation rate constant through both the effects on the

526   side reaction coefficients (Eqs. 7-8) and because the complexes can be non-reactive to

527   oxidation or may oxidize slower than other inorganic species. Moreover, it should be

528   considered that organic matter might even increase the Fe(II) $t_{1/2}$ due to the reduction of

529   organically complexed Fe(III), which would increase the Fe(II) in solution, and therefore the

530     $t_{1/2}$ (Santana-Casiano et al., 2010).

531   The UV-irradiation treatment (Fig. 8) removes the organic matter effect on the Fe-

532   complexation, which for the studied samples resulted in an increase in the oxidation rate

533   constants. Consequently, in these analyzed natural samples, organic matter ultimately

534   lowered the oxidation rate constants (black data points below the straight line in Fig. 9).

535   The DOM is prone to natural and thermal degradation in hydrothermal systems (Hawkes et

536   al., 2016). Accordingly, the variety of organic-complexing ligands and their effect on

537   oxidation could change with plume transport and distance to the vent site as observed in

538   figures 6 and 7. In the proximities to the vent sites, samples presented greater than theoretical

539   oxidation rate constants (above the straight line in Fig. 9). This could be due to the presence

540   of organic matter with ligands complexing Fe that oxidizes faster than the inorganic Fe(II)

541   species. At these locations, the organic ligand effect would dominate over processes that

542   lower oxidation rate constants such as nanoparticle concentrations. Similar experiments

543   considering organic matter degradation just above the vent site should be carried out to

544   confirm this hypothesis. Nevertheless, the complexity of the organic matter pool and the

545   extent and nature of Fe-DOM interactions make the resulting effect on the oxidation rate

546   constants difficult to predict.

547   *4.3. Effects of physical speciation*

548   Lough et al. (2019) have shown that there is an Fe exchange between the different particle

549   size fractions within the hydrothermal plume. This exchange could affect Fe(II) oxidation as

550   found in this study for particles smaller than 0.2 µm and colloidal sized particles (0.2-0.02

551   µm) at different locations in TAG and in Rainbow (Fig. 8). The results shown in Figure 8

552   seem to indicate that the size-fractionation can significantly affect Fe(II) oxidation and thus,

553   is a factor that should be considered in future studies. In this sense, previous work has shown

554   that particulate Fe(II), such as pyrite nanoparticles are more resistant to oxidation, with Fe(II)

24

555 half-life between 4 and 48 months at 2 °C (Yücel et al., 2011). The presence of colloidal

556 particles also enhances the decay of ROS allowing for longer $t_{1/2}$ (Yuan and Shiller, 2001).

557 Therefore, nanoparticles could account for a substantial fraction of the decrease in the

558 oxidation rate constants (Fig. 8). Another consequence of filtration is the reduction in larger

559 size organic matter, which could also affect the stabilization of Fe(II) (Buck et al., 2015).

560 The variability observed in the oxidation rate constants inside the plume for the six studied

561 hydrothermal vents indicates that changes in the composition of both the DOM and colloidal

562 particles, both between sites and at different distances from the vent, can strongly affect the

563 oxidation rate constants, thus, their role requires further study.

5 Conclusions

565 This study highlights the complexity of Fe(II) chemistry in the ocean, with a focus on

566 hydrothermal vent settings. Fe(II) oxidation rate constants, and therefore persistence of Fe(II)

567 in the environment, is shown to not only depend on the physico-chemical conditions (T, S,

568 pH, O_2 content) but also the physical state (soluble, colloidal and particulate) of the inorganic

569 and organic species that are present. Our results indicate that organic ligands can stabilize

570 Fe(II) and that nanoparticles present in hydrothermal plumes could increase the resistance to

571 oxidation. Both processes contribute to the observed variability in the oxidation rate constants

572 in the proximities of vents. We were able to revise the theoretical equation for the estimation

573 of k', and to further increase the existing temperature range to include seawater temperatures

574 as low as 2 ºC. Future studies on iron oxidation kinetics in the marine environment should be

575 accompanied by a characterization of the organic matter present in the medium, a size-

576 fractionation of the samples, and a detailed description of the conventional physico-chemical

577 factors (pH, T, and S).
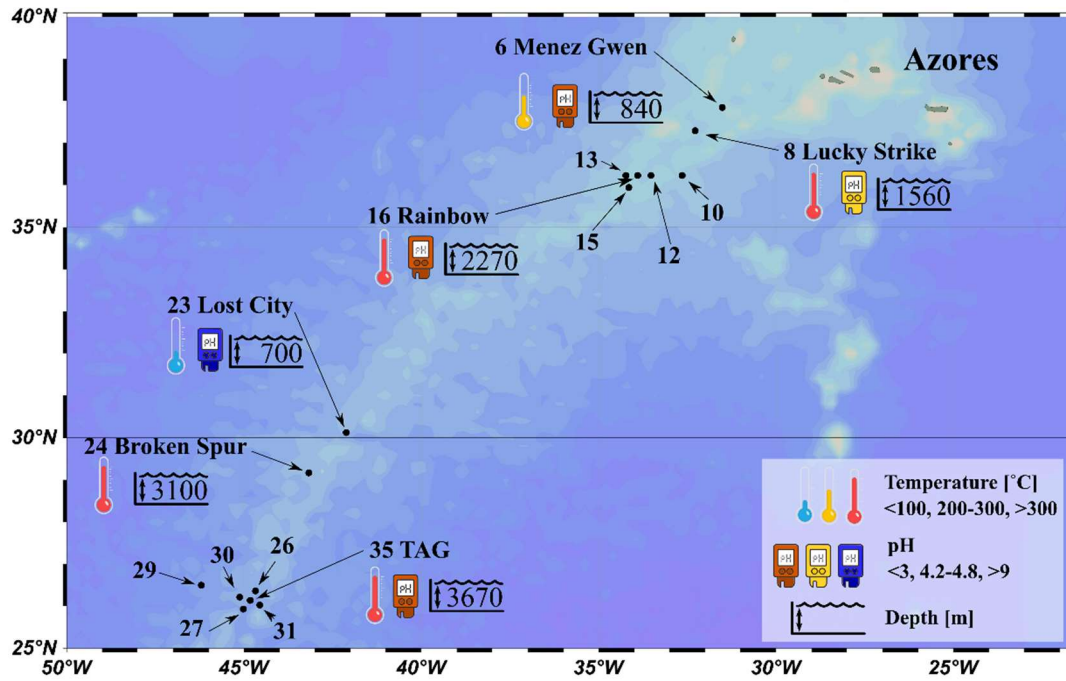
Figures

Figure 1. Map of the investigated hydrothermal vent sites along the MAR, showing the station numbers and hydrothermal vent site names for the sampling sites. Symbols represent endmember characteristics. The pH of the Broken Spur endmember was not available.

583
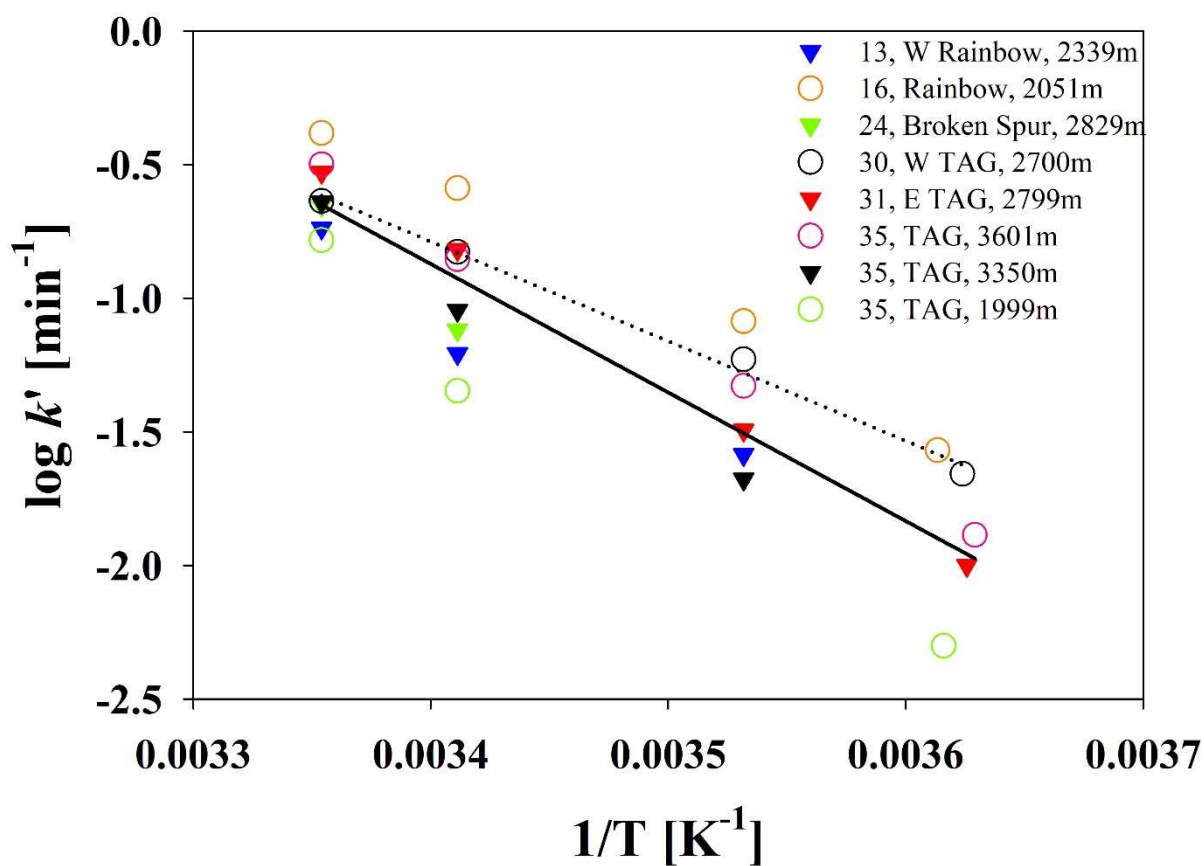
Figure 2. Arrhenius relationship between the oxidation rate constant (log k' (min^{-1})) and

temperature (1/T (K^{-1})) in the range 2 to 25 ºC for eight selected samples. Note that the

sample from station 30 (W TAG, 2700m, open squares, dotted line) shows a different

behavior than samples from other stations.
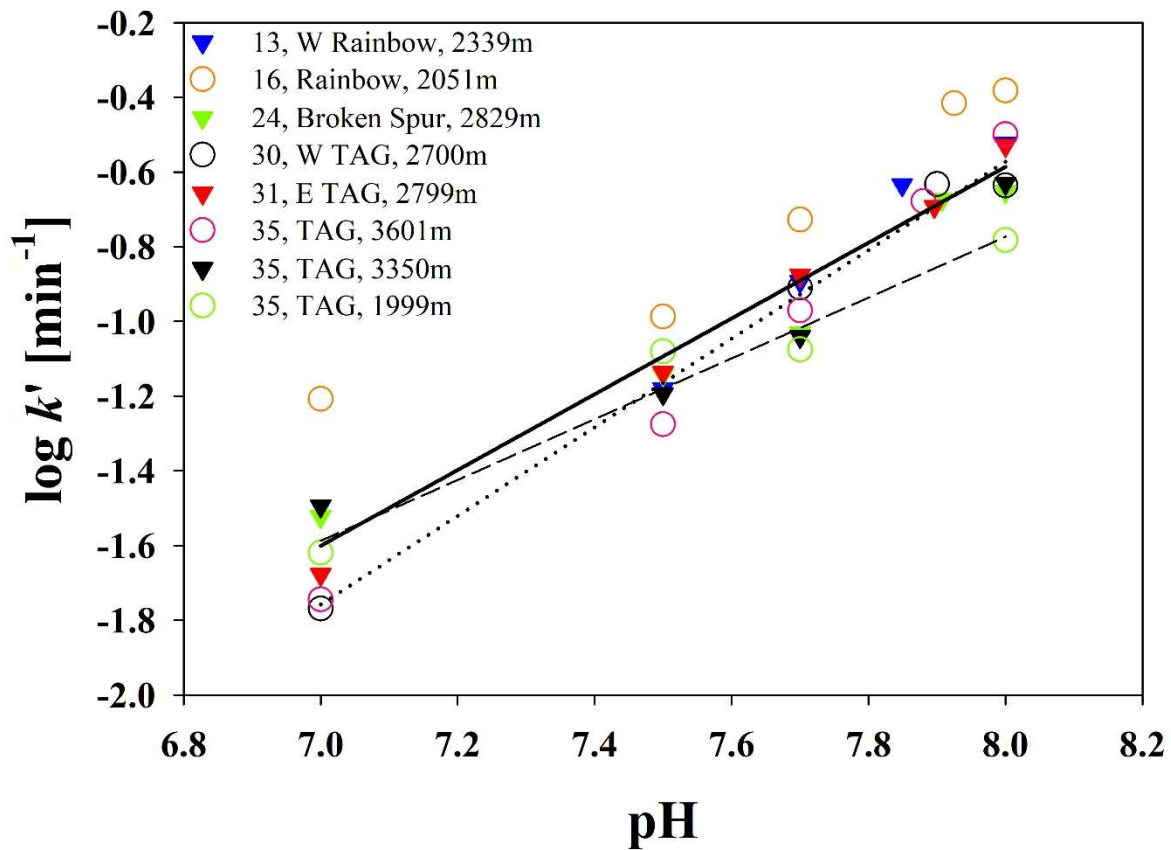
Figure 3. pH effect (from 7.0 to 8.0) on the Fe(II) oxidation rate constants ($\log k'$ (min^{-1})) for eight selected samples collected along the MAR. Note that the samples from 2700 m depth to the west of TAG (Stn 30, open squares) and from 1999 m depth at the TAG site (Stn 35, open diamonds) have different slopes than samples from other stations (data from these two stations are plotted with dotted lines).

594
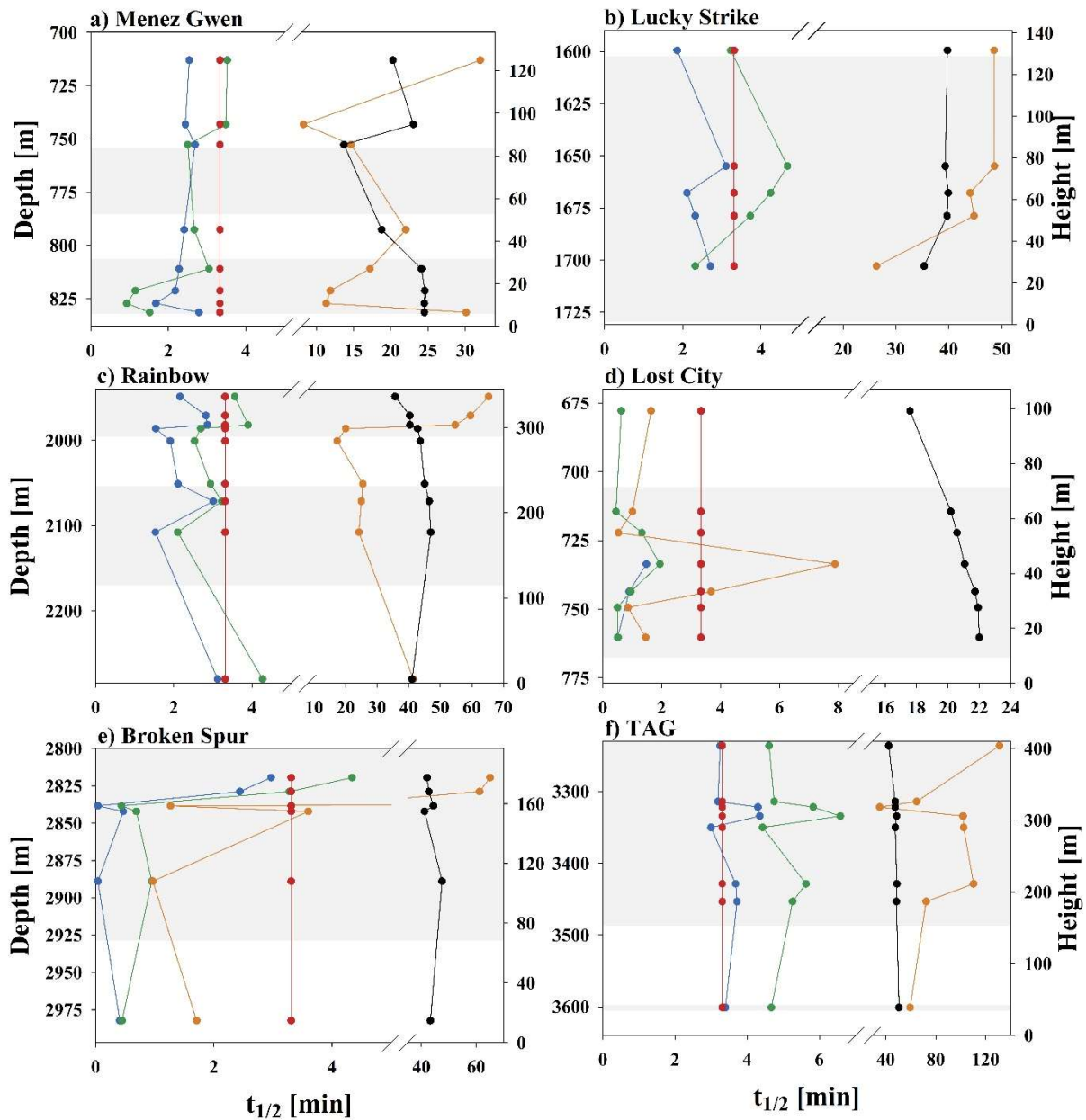
Figure 4. The measured Fe(II) half-life ($t_{1/2}$, min) at $T_{is}pH_{is}$ (orange), $T_{25}pH_{is}$ (green), and

$T_{25}pH_8$ (blue), and the theoretical (Theo) values for $T_{is}pH_{is}$ (black), and $T_{25}pH_8$ (red), at the

six vents. The shaded area shows the anomaly depths determined using light scattering data .

Both, the depth (left y-axis) and the height above the seafloor (right y-axis) of the sampling

are indicated.

600
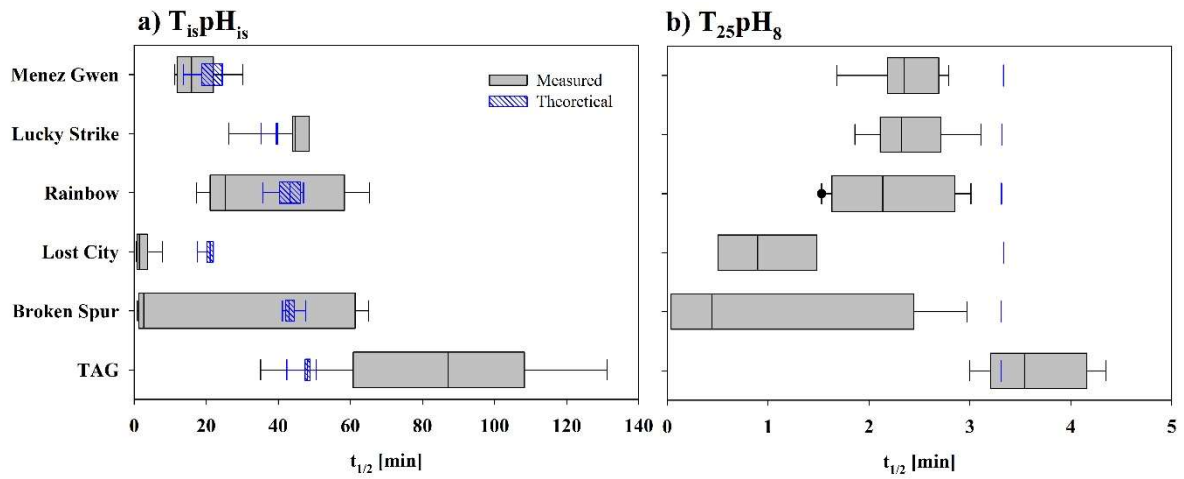
Figure 5. Boxplots of the Fe(II) half-life ($t_{1/2}$, min) within the six hydrothermal plumes. a)
The measured $t_{1/2}$ at *in situ* conditions (grey) and the theoretical $t_{1/2}$ (blue; obtained using Eq.
4). b) The measured $t_{1/2}$ at constant temperature (25 ºC) and pH 8 (grey) and the
corresponding theoretical $t_{1/2}$, the slight variances are caused by S changes (blue).
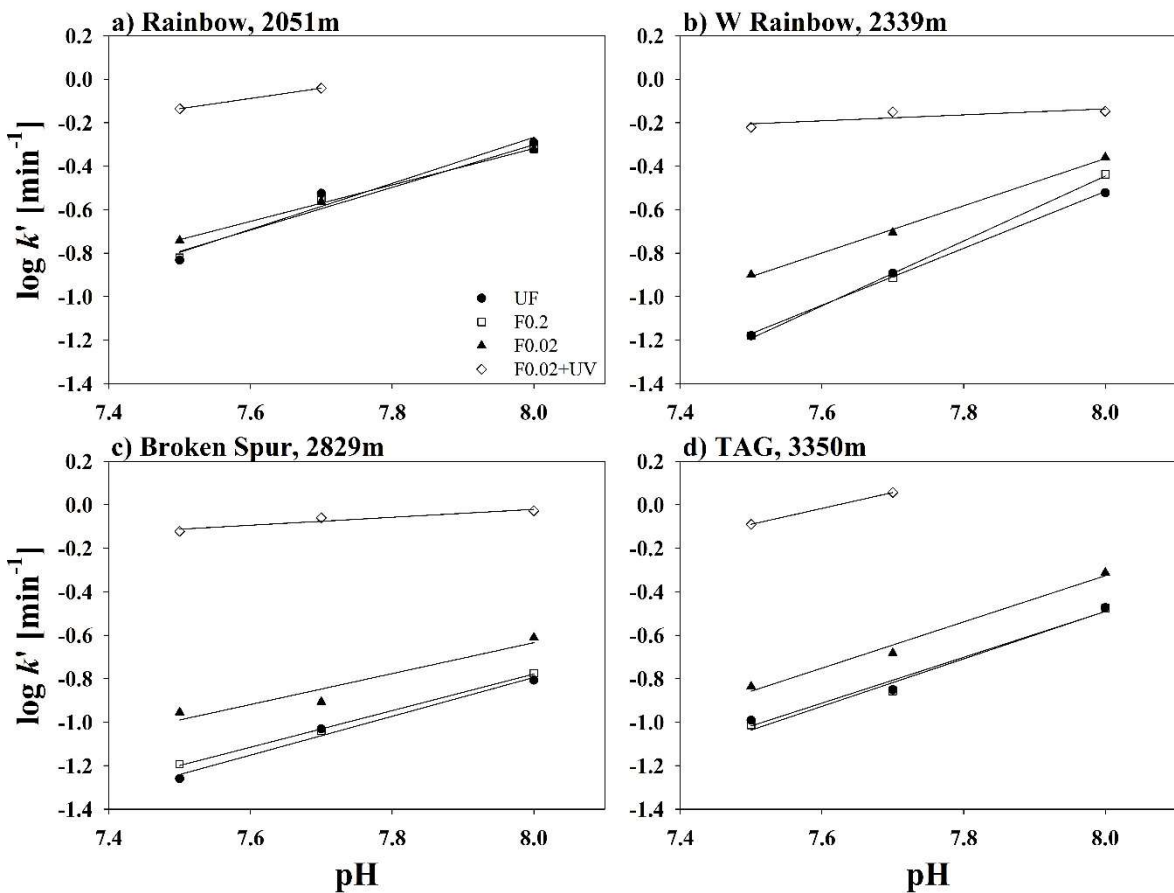

605
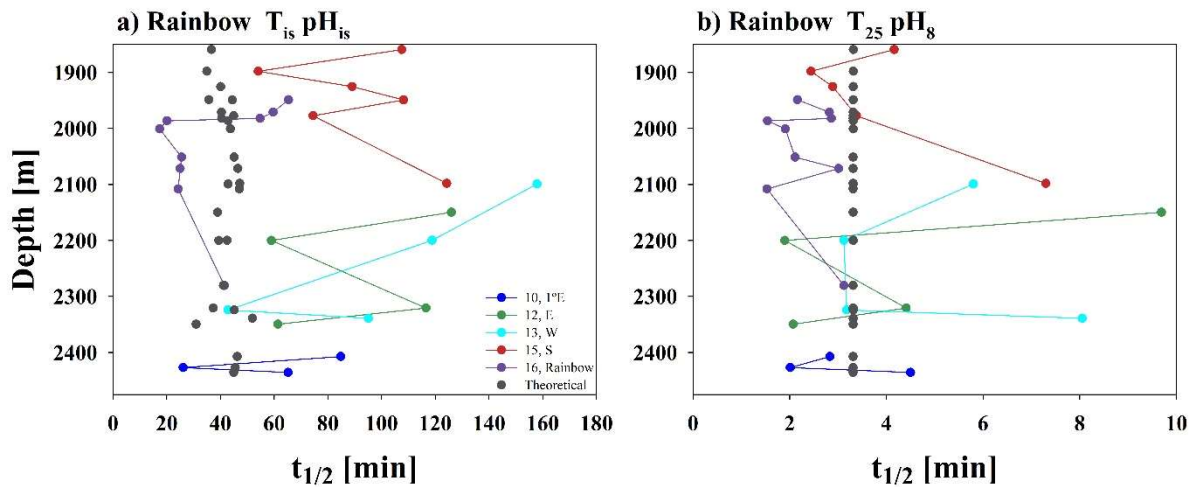
Figure 6. The Fe(II) half-life ($t_{1/2}$, min) at the Rainbow field a) under *in situ* conditions (see
also Supplementary Table S1) and b) normalized to constant T of 25 ºC and a pH of 8.

608
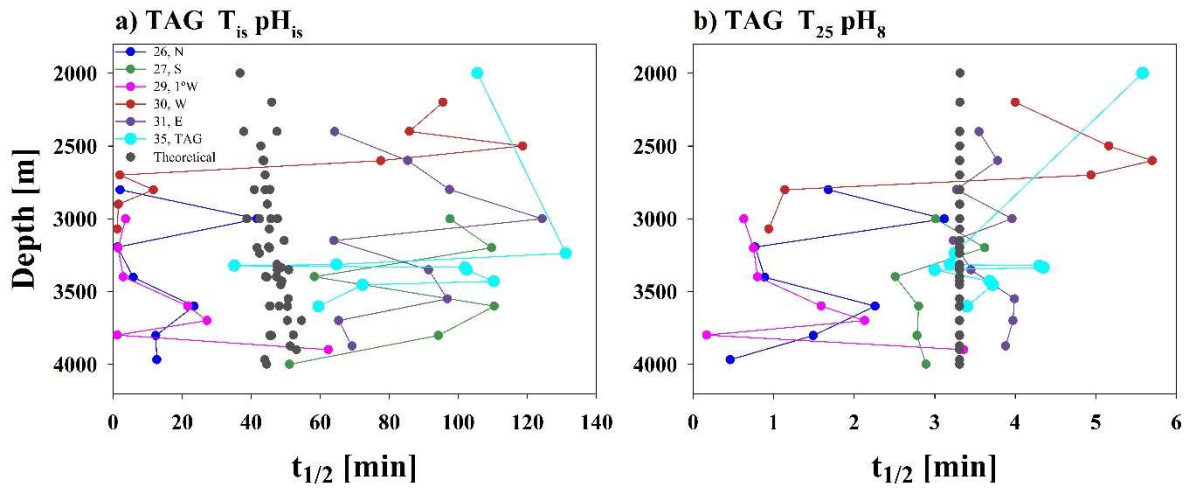
Figure 7. The Fe(II) half-life ($t_{1/2}$, min) at the TAG field a) under *in situ* conditions (see also

Supplementary Table S1) and b) normalized to constant T of 25 ºC and a pH of 8.

611

Figure 8. Oxidation rate constants at different pH (7.5, 7.7 and 8), for selected unfiltered (UF,

filled circles), filtered through 0.2 µm (F0.2, open squares), filtered through 0.02 µm (F0.02,

614   filled triangles) and filtered through 0.02 μm followed by UV irradiation (F0.02+UV, open

615   diamonds) samples at a) Rainbow (Stn 16, 2051 m), b) West of Rainbow (Stn 13, 2339 m), c)

616   Broken Spur (Stn 24, 2829 m) and d) TAG (Stn 35, 3350 m).

617
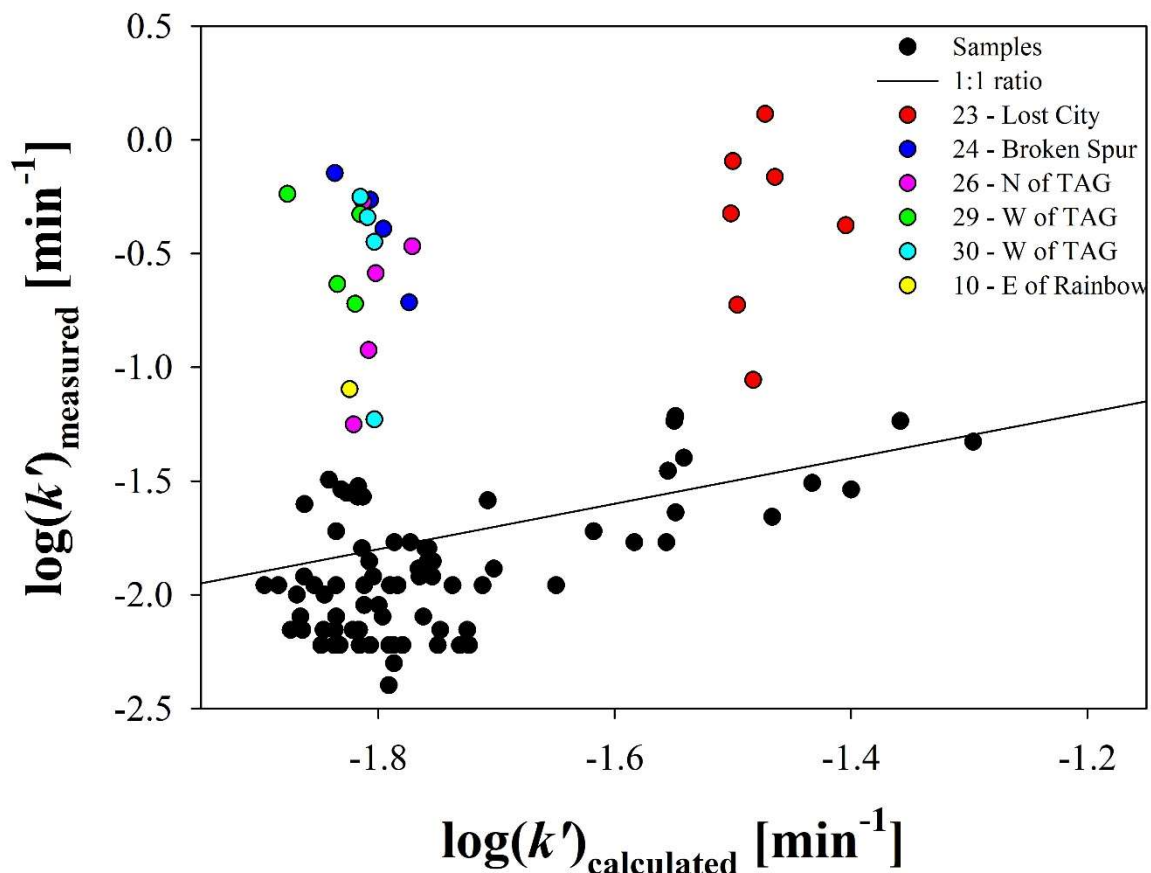
618   Figure 9. Fe(II) oxidation rate constants ($\log(k')$) determined under *in situ* conditions against

619   the anticipated expected theoretical value. All data points are shown in black. The black line

620   represents a 1:1 ratio between both oxidation rate constants. Color coded data points

621   correspond to samples with measured oxidation rate constants greater than 20% of the

622   theoretically derived rate constants.

623   **Author contributions**

624 DGS wrote the manuscript with significant contributions from all coauthors. DGS was

625 invited to the research cruise by MCL and AT, where DGS, MCL, and LA collected the

626 samples. DGS analyzed the samples with support from MSC and MGD. Figures for the

627 results were designed by HP and GS. Fieldwork logistics and costs were overseen by MCL

628 and AT, while analysis costs were handled by MSC, MGD, GS, and HP.

637 **Competing interests**

638 The authors declare no competing interests.

639 **References**

640 Andreani M., Escartin J., Delacour A., Ildefonse B., Godard M., Dyment J., Fallick A. E. and

641   Fouquet Y. (2014) Tectonic structure, lithology, and hydrothermal signature of the

642   Rainbow massif (Mid-Atlantic Ridge 36°14′N). *Geochemistry, Geophys. Geosystems*

643   **15**, 3543–3571.

644 Armstrong R. A., Lee C., Hedges J. I., Honjo S. and Wakeham S. G. (2001) A new,

645   mechanistic model for organic carbon fluxes in the ocean based on the quantitative

646 association of POC with ballast minerals. *Deep Sea Res. Part II Top. Stud. Oceanogr.*

647 **49**, 219–236.

648 de Baar H. J. W. and De Jong J. T. M. (2001) Distributions, sources and sinks of iron in

649 seawater. In *The Biogeochemistry of Iron in Seawater* (eds. D. Turner and K. A.

650 Hunter). John Wiley & Sons Ltd., Chichester, UK. pp. 125–253.

651 Bennett S. A., Achterberg E. P., Connelly D. P., Statham P. J., Fones G. R. and German C. R.

652 (2008) The distribution and stabilisation of dissolved Fe in deep-sea hydrothermal

653 plumes. *Earth Planet. Sci. Lett.* **270**, 157–167.

654 Buck K. N., Sohst B. and Sedwick P. N. (2015) The organic complexation of dissolved iron

655 along the U.S. GEOTRACES (GA03) North Atlantic Section. *Deep Sea Res. Part II*

656 *Top. Stud. Oceanogr.* **116**, 152–165.

657 Bundy R. M., Biller D. V, Buck K. N., Bruland K. W. and Barbeau K. A. (2014) Distinct

658 pools of dissolved iron-binding ligands in the surface and benthic boundary layer of the

659 California Current. *Limnol. Oceanogr.* **59**, 769–787.

660 Charlou J. L., Donval J. P., Douville E., Jean-Baptiste P., Radford-Knoery J., Fouquet Y.,

661 Dapoigny A. and Stievenard M. (2000) Compared geochemical signatures and the

662 evolution of Menez Gwen (35°50N) and Lucky Strike (37°17N) hydrothermal fluids,

663 south of the Azores Triple Junction on the Mid-Atlantic Ridge. *Chem. Geol.* **171**, 49–75.

664 Chin C. S., Coale K. H., Elrod V. A., Johnson K. S., Massoth G. J. and Baker E. T. (1994) In

665 situ observations of dissolved iron and manganese in hydrothermal vent plumes, Juan de

666 Fuca Ridge. *J. Geophys. Res. Solid Earth* **99**, 4969–4984.

667 Conway T. J. and John S. G. (2014) Quantification of dissolved iron sources to the North

668   Atlantic Ocean. *Nature* **511**, 212–215.

669   Douville E., Charlou J. L., Oelkers E. H., Bienvenu P., Jove Colon C. F., Donval J. P.,

670   Fouquet Y., Prieur D. and Appriou P. (2002) The rainbow vent fluids (36°14′N, MAR):

671   The influence of ultramafic rocks and phase separation on trace metal content in Mid-

672   Atlantic Ridge hydrothermal fluids. *Chem. Geol.* **184**, 37–48.

673   Elderfield H. and Schultz A. (1996) Mid-ocean ridge hydrothermal fluxes and the chemical

674   composition of the ocean. *Annu. Rev. Earth Planet. Sci.* **24**, 191–224.

675   Field M. P. and Sherrell R. M. (2000) Dissolved and particulate Fe in a hydrothermal plume

676   at 9°45'N, East Pacific Rise: Slow Fe (II) oxidation kinetics in Pacific plumes. *Geochim.*

677   *Cosmochim. Acta* **64**, 619–628.

678   Fitzsimmons J. N., John S. G., Marsay C. M., Hoffman C. L., Nicholas S. L., Toner B. M.,

679   German C. R. and Sherrell R. M. (2017) Iron persistence in a distal hydrothermal plume

680   supported by dissolved-particulate exchange. *Nat. Geosci.* **10**, 195–201.

681   Fouquet Y., Cambon P., Etoubleau J., Charlou J. L., Ondréas H., Barriga F. J. A. S.,

682   Cherkashov G., Semkova T., Poroshina I., Bohn M., Donval J. P., Henry K., Murphy P.

683   and Rouxel O. (2013) Geodiversity of hydrothermal processes along the mid-atlantic

684   ridge and ultramafic-hosted mineralization: A new type of oceanic Cu-Zn-Co-Au

685   volcanogenic massive sulfide deposit. *Geophys. Monogr. Ser.* **188**, 321–367.

686   Gamo T., Chiba H., Masuda H., Edmonds H. N., Fujioka K., Kodama Y., Nanba H. and Sano

687   Y. (1996) Chemical characteristics of hydrothermal fluids from the TAG Mound of the

688   Mid-Atlantic Ridge in August 1994: Implications for spatial and temporal variability of

689   hydrothermal activity. *Geophys. Res. Lett.* **23**, 3483–3486.

690   Gartman A. and Findlay A. J. (2020) Impacts of hydrothermal plume processes on oceanic

691   metal cycles and transport. *Nat. Geosci.* **13**, 396–402.

692   German C. R. and Von Damm K. L. (2004) Hydrothermal processes. In *The Oceans and*

693   *Marine Geochemistry* (eds. H. D. Holland, K. K. Turekian, and H. Elderfield). Elsevier-

694   Pergamon. pp. 181–222.

695   Gledhill M. and Buck K. (2012) The Organic Complexation of Iron in the Marine

696   Environment: A Review. *Front. Microbiol.* **3**, 69.

697   González-Davila M., Santana-Casiano J. M. and Millero F. J. (2005) Oxidation of iron (II)

698   nanomolar with H_2O_2 in seawater. *Geochim. Cosmochim. Acta* **69**, 83–93.

699   González-Dávila M., Santana-Casiano J. M. and Millero F. J. (2006) Competition between O_2

700   and H_2O_2 in the oxidation of Fe (II) in natural waters. *J. Solution Chem.* **35**, 95–111.

701   Gray S. E. C., DeGrandpre M. D., Moore T. S., Martz T. R., Friederich G. E. and Johnson K.

702   S. (2011) Applications of in situ pH measurements for inorganic carbon calculations.

703   *Mar. Chem.* **125**, 82–90.

704   Hawkes J. A., Hansen C. T., Goldhammer T., Bach W. and Dittmar T. (2016) Molecular

705   alteration of marine dissolved organic matter under experimental hydrothermal

706   conditions. *Geochim. Cosmochim. Acta* **175**, 68–85.

707   Hong H. and Kester D. R. (1986) Redox state of iron in the offshore waters of Peru[1]. *Limnol.*

708   *Oceanogr.* **31**, 512–524.

709   James R. H., Elderfield H. and Palmer M. R. (1995) The chemistry of hydrothermal fluids

710   from the Broken Spur site, 29 N Mid-Atlantic Ridge. *Geochim. Cosmochim. Acta* **59**,

711   651–659.

712 Kelley D. S., Karson J. A., Blackman D. K., Früh-Green G. L., Butterfield D. A., Lilley M.

713   D., Olson E. J., Schrenk M. O., Roe K. K. and Lebon G. T. (2001) An off-axis

714   hydrothermal vent field near the Mid-Atlantic Ridge at 30 N. *Nature* **412**, 145–149.

715 Key R. M., Olsen A., van Heuven S., Lauvset S. K., Velo A., Lin X., Schirnick C., Kozyr A.,

716   Tanhua T. and Hoppema M. (2015) Global ocean data analysis project, version 2

717   (GLODAPv2).

718 King D. W. (1998) Role of carbonate speciation on the oxidation rate of Fe (II) in aquatic

719   systems. *Environ. Sci. Technol.* **32**, 2997–3003.

720 King D. W., Lounsbury H. A. and Millero F. J. (1995) Rates and Mechanism of Fe(II)

721   Oxidation at Nanomolar Total Iron Concentrations. *Environ. Sci. Technol.* **29**, 818–824.

722 Lough A. J. M., Homoky W. B., Connelly D. P., Comer-Warner S. A., Nakamura K.,

723   Abyaneh M. K., Kaulich B. and Mills R. A. (2019) Soluble iron conservation and

724   colloidal iron dynamics in a hydrothermal plume. *Chem. Geol.* **511**, 225–237.

725 Ludwig K. A., Kelley D. S., Butterfield D. A., Nelson B. K. and Früh-Green G. L. (2006)

726   Formation and evolution of carbonate chimneys at the Lost City Hydrothermal Field.

727   *Geochim. Cosmochim. Acta* **70**, 3625–3645.

728 Lueker T. J., Dickson A. G. and Keeling C. D. (2000) Ocean pCO$_2$ calculated from dissolved

729   inorganic carbon, alkalinity, and equations for K$_1$ and K$_2$: validation based on laboratory

730   measurements of CO$_2$ in gas and seawater at equilibrium. *Mar. Chem.* **70**, 105–119.

731 Mandernack K. W. and Tebo B. M. (1993) Manganese scavenging and oxidation at

732   hydrothermal vents and in vent plumes. *Geochim. Cosmochim. Acta* **57**, 3907–3923.

733 Massoth G. J., Baker E. T., Feely R. A., Lupton J. E., Collier R. W., Gendron J. F., Roe K.

734   K., Maenner S. M. and Resing J. A. (1998) Manganese and iron in hydrothermal plumes

735   resulting from the 1996 Gorda Ridge Event. *Deep Sea Res. Part II Top. Stud. Oceanogr.*

736   **45**, 2683–2712.

737   Massoth G. J., Baker E. T., Lupton J. E., Feely R. A., Butterfield D. A., Von Damm K. L.,

738   Roe K. K. and Lebon G. T. (1994) Temporal and spatial variability of hydrothermal

739   manganese and iron at Cleft segment, Juan de Fuca Ridge. *J. Geophys. Res. Solid Earth*

740   **99**, 4905–4923.

741   Millero F. J. (1986) The pH of estuarine waters. *Limnol. Oceanogr.* **31**, 839–847.

742   Millero F. J. and Sotolongo S. (1989) The oxidation of Fe (II) with H_2O_2 in seawater.

743   *Geochim. Cosmochim. Acta* **53**, 1867–1873.

744   Millero F. J., Sotolongo S. and Izaguirre M. (1987) The oxidation kinetics of Fe(II) in

745   seawater. *Geochim. Cosmochim. Acta* **51**, 793–801.

746   Millero F. J., Yao W. and Aicher J. (1995) The speciation of Fe (II) and Fe (III) in natural

747   waters. *Mar. Chem.* **50**, 21–39.

748   Moore C. M., Mills M. M., Arrigo K. R., Berman-Frank I., Bopp L., Boyd P. W., Galbraith

749   E. D., Geider R. J., Guieu C., Jaccard S. L., Jickells T. D., La Roche J., Lenton T. M.,

750   Mahowald N. M., Marañón E., Marinov I., Moore J. K., Nakatsuka T., Oschlies A.,

751   Saito M. A., Thingstad T. F., Tsuda A. and Ulloa O. (2013) Processes and patterns of

752   oceanic nutrient limitation. *Nat. Geosci.* **6**, 701–710.

753   Morel F. M. M., Kustka A. B. and Shaked Y. (2008) The role of unchelated Fe in the iron

754   nutrition of phytoplankton. *Limnol. Oceanogr.* **53**, 400–404.

755   Moriceau B., Goutx M., Guigue C., Lee C., Armstrong R., Duflos M., Tamburini C.,

756   Charrière B. and Ragueneau O. (2009) Si–C interactions during degradation of the

757   diatom Skeletonema marinoi. *Deep Sea Res. Part II Top. Stud. Oceanogr.* **56**, 1381–

758   1395.

759   Mottl M. J., Holland H. D. and Corr R. F. (1979) Chemical exchange during hydrothermal

760   alteration of basalt by seawater-II. Experimental results for Fe, Mn, and sulfur species.

761   *Geochim. Cosmochim. Acta* **43**, 869–884.

762   O'Sullivan D. W., Neale P. J., Coffin R. B., Boyd T. J. and Osburn C. L. (2005)

763   Photochemical production of hydrogen peroxide and methylhydroperoxide in coastal

764   waters. *Mar. Chem.* **97**, 14–33.

765   Olsen A., Key R. M., Van Heuven S., Lauvset S. K., Velo A., Lin X., Schirnick C., Kozyr A.,

766   Tanhua T. and Hoppema M. (2016) The Global Ocean Data Analysis Project version 2

767   (GLODAPv2)–an internally consistent data product for the world ocean. *Earth Syst. Sci.*

768   *Data* **8**.

769   Resing J. A., Sedwick P. N., German C. R., Jenkins W. J., Moffett J. W., Sohst B. M. and

770   Tagliabue A. (2015) Basin-scale transport of hydrothermal dissolved metals across the

771   South Pacific Ocean. *Nature* **523**, 200–203.

772   Rose A. L. and Waite T. D. (2003) Effect of dissolved natural organic matter on the kinetics

773   of ferrous iron oxygenation in seawater. *Environ. Sci. Technol.* **37**, 4877–4886.

774   Rouxel O., Toner B., Germain Y. and Glazer B. (2018) Geochemical and iron isotopic

775   insights into hydrothermal iron oxyhydroxide deposit formation at Loihi Seamount.

776   *Geochim. Cosmochim. Acta* **220**, 449–482.

777   Roy E. G. and Wells M. L. (2011) Evidence for regulation of Fe (II) oxidation by organic

778   complexing ligands in the Eastern Subarctic Pacific. *Mar. Chem.* **127**, 115–122.

779   Roy E. G., Wells M. L. and King D. W. (2008) Persistence of iron (II) in surface waters of

780   the western subarctic Pacific. *Limnol. Oceanogr.* **53**, 89–98.

781   Rudnicki M. D. and Elderfield H. (1993) A chemical model of the buoyant and neutrally

782   buoyant plume above the TAG vent field, 26 degrees N, Mid-Atlantic Ridge. *Geochim.*

783   *Cosmochim. Acta* **57**, 2939–2957.

784   Rue E. L. and Bruland K. W. (1995) Complexation of iron(III) by natural organic ligands in

785   the Central North Pacific as determined by a new competitive ligand

786   equilibration/adsorptive cathodic stripping voltammetric method. *Mar. Chem.* **50**, 117–

787   138.

788   Santana-Casiano J. M., González-Dávila M., González A. G. and Millero F. J. (2010) Fe (III)

789   reduction in the presence of catechol in seawater. *Aquat. geochemistry* **16**, 467–482.

790   Santana-Casiano J. M., González-Dávila M. and Millero F. J. (2005) Oxidation of nanomolar

791   level of Fe(II) with oxygen in natural waters. *Environ. Sci. Technol.* **39**, 2073–2079.

792   Santana-Casiano J. M., González-Dávila M. and Millero F. J. (2006) The role of Fe(II)

793   species on the oxidation of Fe(II) in natural waters in the presence of O_2 and H_2O_2. *Mar.*

794   *Chem.* **99**, 70–82.

795   Santana-Casiano J. M., González-Dávila M., Rodríguez M. J. and Millero F. J. (2000) The

796   effect of organic compounds in the oxidation kinetics of Fe(II). *Mar. Chem.* **70**, 211–

797   222.

798   Santana-González C., González-Dávila M., Santana-Casiano J. M., Gladyshev S. and Sokov

799   A. (2019) Organic matter effect on Fe (II) oxidation kinetics in the Labrador Sea. *Chem.*

800   *Geol.* **511**, 238–255.

801   Santana-González C., Santana-Casiano J. M., González-Dávila M. and Fraile-Nuez E. (2017)

802   Emissions of Fe(II) and its kinetic of oxidation at Tagoro submarine volcano, El Hierro.

803   *Mar. Chem.* **195**, 129–137.

804   Santana-González C., Santana-Casiano J. M., González-Dávila M., Santana-del Pino A.,

805   Gladyshev S. and Sokov A. (2018) Fe (II) oxidation kinetics in the North Atlantic along

806   the 59.5° N during 2016. *Mar. Chem.* **203**, 64–77.

807   Searle R. (2013) *Mid-ocean ridges*., Cambridge University Press.

808   Shaked Y., Kustka A. B. and Morel F. M. M. (2005) A general kinetic model for iron

809   acquisition by eukaryotic phytoplankton. *Limnol. Oceanogr.* **50**, 872–882.

810   Statham P. J., German C. R. and Connelly D. P. (2005) Iron (II) distribution and oxidation

811   kinetics in hydrothermal plumes at the Kairei and Edmond vent sites, Indian Ocean.

812   *Earth Planet. Sci. Lett.* **236**, 588–596.

813   Stumm W. and Lee G. F. (1961) Oxygenation of ferrous iron. *Ind. Eng. Chem.* **53**, 143–146.

814   Tagliabue A., Bopp L., Dutay J. C., Bowie A. R., Chever F., Jean-Baptiste P., Bucciarelli E.,

815   Lannuzel D., Remenyi T., Sarthou G., Aumont O., Gehlen M. and Jeandel C. (2010)

816   Hydrothermal contribution to the oceanic dissolved iron inventory. *Nat. Geosci.* **3**, 252–

817   256.

818   Tagliabue A., Bowie A. R., Boyd P. W., Buck K. N., Johnson K. S. and Saito M. A. (2017)

819   The integral role of iron in ocean biogeochemistry. *Nature* **543**, 51–59.

820   Tagliabue A. and Völker C. (2011) Towards accounting for dissolved iron speciation in

821   global ocean models. *Biogeosciences* **8**, 3025–3039.

822 Ussher S. J., Achterberg E. P. and Worsfold P. J. (2004) Marine biogeochemistry of iron.

823   *Environ. Chem.* **1**, 67–80.

824 Voelker B. M. and Sedlak D. L. (1995) Iron reduction by photoproduced superoxide in

825   seawater. *Mar. Chem.* **50**, 93–102.

826 Voelker B. M. and Sulzberger B. (1996) Effects of fulvic acid on Fe (II) oxidation by

827   hydrogen peroxide. *Environ. Sci. Technol.* **30**, 1106–1114.

828 Wang H., Yang Q., Ji F., Lilley M. D. and Zhou H. (2012) The geochemical characteristics

829   and Fe (II) oxidation kinetics of hydrothermal plumes at the Southwest Indian Ridge.

830   *Mar. Chem.* **134**, 29–35.

831 Yuan J. and Shiller A. M. (2001) The distribution of hydrogen peroxide in the southern and

832   central Atlantic ocean. *Deep Sea Res. Part II Top. Stud. Oceanogr.* **48**, 2947–2970.

833 Yücel M., Gartman A., Chan C. S. and Luther G. W. (2011) *Hydrothermal vents as a*

834   *kinetically stable source of iron-sulphide-bearing nanoparticles to the ocean.*, Nature

835   Publishing Group.

836